Experimental and theoretical analyses of a correlation between pump-pulse propagation and harmonic yield in a long-interaction medium

Eiji Takahashi,* Valer Tosa,† Yasuo Nabekawa, and Katsumi Midorikawa‡
Laser Technology Laboratory, RIKEN, 2-1 Hirosawa, Wako, Saitama 351-0198, Japan
(Received 12 February 2003; published 22 August 2003)

We performed experimental and theoretical analyses of a correlation between pump pulse propagation and harmonic yield in Ar and Xe, in a long static gas cell, at high pumping energies, for loose focusing geometry, using 35-fs pulses from a Ti:sapphire laser. Axial and transverse profiles of the plasma column were measured under several experimental conditions with the aim of characterizing the pulse propagation. From the plasma fluorescence profiles observed, it was found that self-guided propagation of the pump pulse in Xe resulted in the channel formation. A three-dimensional nonadiabatic propagation model was used to calculate the field configuration in the interaction region and to explain the channel formation. A model developed to calculate the transverse plasma profiles can adequately reproduce the experimental data and confirm the channel formation. Correlated measurements of harmonics generation reveal that channel formation greatly enhances the harmonic yield as harmonics propagate under phase-matched conditions.

DOI: 10.1103/PhysRevA.68.023808 PACS number(s): 42.65.Ky, 32.80.Rm, 52.38.Hb

I. INTRODUCTION

Recently, theoretical predictions of nonlinear interaction between soft x rays and matter have been reported by a few groups, such as two-photon ionization of He^+ [1], He double ionization for the autocorrelation of an extreme-ultraviolet (XUV) pulse [2], the advantages of high-intensity short-wavelength radiation for Coulomb explosion imaging [3], and ionization of cluster target [4]. The above research field can be expected to open a new area in high-intensity physics. However, to observe such nonlinear effects, generation of the strong optical field in the XUV region is indispensable. For example, as Ishikawa and Midorikawa pointed out, the observation of two-photon ionization of He^+ by a 30-nm pulse requires a light intensity of higher than 10^{13} W/cm^2 [1].

To make a breakthrough in nonlinear physics in the soft-x-ray region, one of the most important issues is the development of high-intensity coherent soft-x-ray light sources. At present, a new x-ray free electron laser (XFEL) at the TESLA Test Facility at the Deusches Elektronen-Synchrotron (DESY) has successfully generated a vacuum ultraviolet (VUV) pulse in the wavelength region around 98 nm with an output energy of 35 μJ/pulse and a pulse width of 100 fs at 1-Hz repetition [5]. If the upgrading of the DESY goes well, an high-energy soft-x-ray pulse will be available in the future. On the other hand, a high-order harmonic (HH) process [6,7] can generate highly coherent short-wavelength lights in the VUV to soft-x-ray region. Compared with XFEL, HH has many advantages such as ultrashort pulse duration, wide tunability, high repetition rate, ease of handling, and low equipment cost. This emission source has been used as a diagnostic tool in solid-state and plasma physics as well as atomic and molecular spectroscopy, and for the generation of attosecond pulses [8]. Recently, research into high-order harmonic generation (HHG) has focused on increasing the output harmonic energy. Takahashi *et al.* reported the energy scaling of HH under the phase-matched condition using a long-interaction length and a loosely focused beam in Ar [9,10]. In that experiment, the total output energy attained in the spectral region from 34.8 to 25.8 nm (the corresponding order of 23rd to 31st) was $\sim$0.7 μJ, and the maximal 27th harmonic (29.6 nm) energy was found to be 0.32 μJ with 0.7 mrad (full width at half maximum, FWHM) beam divergence. In addition, the microjoule level harmonic energy in the XUV region was obtained by a number of groups [11–14]; in the low-order perturbative region, Dolle *et al.* [13] achieved an output energy of 100 μJ at 82.8 nm (3rd harmonic of a KrF laser), and Yoshitomi *et al.* [14] recently reported an average power of submilliwatt at 49.7 nm (5th harmonic) pulses with a 200-Hz KrF laser. To realize a soft-x-ray nonlinear physics generated by HH, the establishment and development of an HH energy scaling strategy is very important.

Recently, our research group reported an HH energy scaling strategy under the phase-matched condition using a Ti:sapphire laser [9–11]. Our scaling method is very simple in principle (see Sec. II A), and has demonstrated a linear increase of harmonic energy with respect to the geometrical focusing area of the pump pulse. We also found that our method is applicable to HHG in several rare gases [11]. In our energy scale-up procedure, we found that the conversion efficiency of HH was improved when we increased the interaction length. In Ar [9,10], using long focusing, the conversion efficiency of the 27th harmonic (29.6 nm) was improved by a factor of 2 compared with the short-focusing condition, and attained a value of 1.5×10^{-5}. Similarly, in Xe, the maximal conversion efficiency of the 15th harmonic (53 nm) obtained with a 5-m focusing lens is 6×10^{-5} [11], which corresponds to an improvement by a factor of 1.6 over a previous result [15] obtained with a 0.5 m focal length. Also,

*Electronic address: e-taka@postman.riken.go.jp
†On leave from The National Institute for R&D in Isotopic and Molecular Technologies, Cluj-Napoca, Romania.
‡Electronic address: kmidori@postman.riken.go.jp

Hergott *et al.* reported a sixfold improvement of the conversion efficiency for the 15th harmonic with a 5-m focusing lens and a long gas-jet target, compared with a 2-m focusing lens [12]. These efficiency improvements were qualitatively explained by pump pulse guiding due to the balance between defocusing and self-focusing in the target medium [10,12]. However, details of the physical mechanism by which the HH output to the pump propagation in the interaction region have not been investigated.

In this study, to gain an understanding of the improvement of HH conversion efficiency with a loosely focused beam and a long-interaction medium, we comprehensively investigated the relationship between output HH intensity and the propagation condition of the pump pulse in a target medium. Important information on pulse propagation dynamics can be extracted from the plasma fluorescence column [16], which we can observe directly during experiments by means of a charge-coupled device (CCD) camera. In addition, to explain the data and the relationship between the HHG and plasma column structure, we used a nonadiabatic 3D model [17] to study the pulse propagation in the few optical cycles regime.

First, we describe the energy scaling strategy of HH in Sec. II A. Sections II B and II C are devoted to the experimental setup and typical measurement results of HH and the plasma column. In Sec. II E, we show the experimental results for the relationship between the plasma column structure and the HH signal. Section III presents the numerical model used for pulse propagation and for fluorescence modeling. The results of the calculations are shown and discussed in Sec. IV. Finally, we summarize our experimental and simulation results.

II. EXPERIMENTAL RESULTS

A. Strategy for energy scaling of HH

As has been reported in a previous publication [15], to increase the HH yield, the coherence length L_{coh} should be much longer than the absorption length L_{abs} for a given harmonic order q. The coherence length is given by $\pi/\Delta k$, where $\Delta k = k_q - qk_0$ indicates the amount of phase mismatch between the harmonic field and the atomic dipoles. k_q and k_0 are wave vectors which correspond to the phase velocity of the harmonic field and atomic dipole, respectively. When the coherence length is comparable to the absorption length, the HH yield saturates as soon as the medium length becomes longer than the absorption length. To achieve the phase matching, the contributions due to neutral atoms, free electrons, and geometrical dispersions must be balanced. If the condition $L_{\mathrm{coh}} \gg L_{\mathrm{abs}}$ holds, the maximum harmonic yield is accomplished with an interaction length L_{int} that is three times longer [15] than the absorption length. To extend the interaction length between the laser pulse and the target medium, the Rayleigh length must be extended. Increasing the Rayleigh length leads to the increase in the spot size of the pump pulse. This allows one to increase the pump pulse energy, which is indispensable for high-energy output. Our scaling method demonstrated a linear increase in harmonic energy with respect to the geometrical focusing area of the pump pulse, while keeping an almost perfect spatial profile of the harmonic output [10].

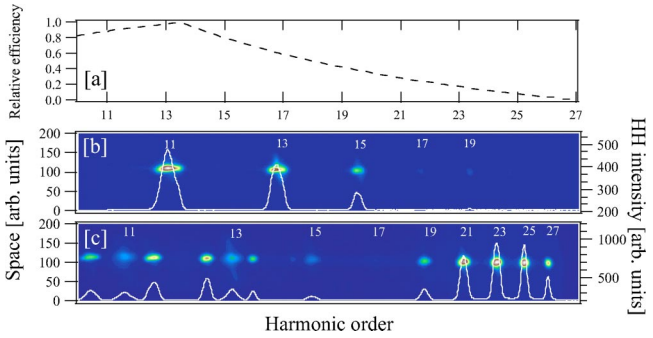

FIG. 1. (Color online) Optimized HH spectrum by 50-shots accumulation from Ar (c) and Xe (b). The top panel (a) shows the relative efficiency with a flat-field normal-incidence XUV spectrometer with a platinum-coated concave grating blazed at 60 nm (1200 lines/mm).

B. Experimental setup

In the experiment, to increase both the interaction length and the pump pulse energy, a loosely focused pumping geometry with an $f=5000$-mm planoconvex lens was employed. The pump pulse was supplied by a 10-Hz Ti:sapphire laser system based on chirped pulse amplification. In this system, the pulse width was 35 fs and the wavelength was centered at 800 nm. The pump pulse was loosely focused, and delivered into the target chamber through a CaF_2 window. First, we set the focus around the entrance pinhole of the interaction cell. The interaction cell had two pinholes on each end surface of the bellow arms. The diameter of the pinholes was 1.2 mm. These pinholes isolated the vacuum and gas-filled regions. The interaction length was variable from 0 to 150 mm in the interaction cell. Target gas was statically filled in the interaction cell. The generated harmonics illuminated a 150 μm $(H)\times 12$ mm (V) slit of the spectrometer. Harmonic signals were observed with a flat-field normal-incident XUV spectrometer with a platinum-coated concave grating blazed at 60 nm (1200 lines/mm). The relative efficiency of the grating is shown in the top figure of Fig. 1. This spectrometer equipped with a microchannel plate (MCP) can cover the spectral range from 30 to 80 nm. A CCD camera detected two-dimensional fluorescence from a phosphor screen placed behind the MCP. Therefore, we measured the spectrally resolved far-field HH profile. The absolute energy of HH was measured directly with an unbiased silicon XUV photodiode. This detector has a wide range of sensitivity from 200 nm to 0.07 nm (6 eV to 17.6 keV). The sensitivity of this photodiode follows the simple linear law $N_e = E_{\mathrm{ph}}/3.63$ eV, where N_e is the number of photoelectrons created by a single XUV photon of energy E_{ph}.

To investigate the detailed structure of visible fluorescence from the plasma, we used two measurement optical systems. One system had a wide-angle optical range for the measurement of global imaging (6 cm$\times$6 cm), and the spatial resolution was estimated to be $\sim$200 μm. The second

optical system had a high spatial resolution, which was estimated to be ~15 μm, and the measurement spatial size was 2.5×2.5 mm. To eliminate the scattered pump pulse light, an IR mirror was set behind the imaging lens. In addition, one basic item of information which we needed, the time dependence of the fluorescence signal, was measured by using a fast photodiode and a BG40 filter which is transparent in the 300–700 nm spectral region. The temporal resolution of this system was estimated to be less than 4 ns.

C. Typical HH signal and plasma column

Figure 1 depicts a typical HH far-field spectrum distribution from Xe and Ar gases. Figure 1(a) shows the grating relative efficiency of the spectrometer. In Figs. 1(b) and 1(c), the horizontal axis denotes the harmonic order, the left vertical axis denotes the space, and the right axis corresponds to the integrated harmonic signal.

A typical HH spectrum for the interaction length, $L_{\mathrm{int}}=14$ cm and 0.6 Torr Xe is shown in Fig. 1(b). The pump pulse energy and the truncated diameter were set at 10 mJ and 14 mm, respectively. The spot size ($1/e$ radius) of the pump pulse at the focus was measured to be 210 μm with an attenuated pump pulse having a beam diameter of 14 mm. In a first approximation, one can assume that the Gouy phase and the dipole phase are balanced by the negative dispersion of the target gas. Since the Gouy phase is given by $\Delta k_{\mathrm{gouy}}(z)=q/(z_0+z^2/z_0^2)$, the geometrical phase shift was estimated to be $5.85\times10^{-2}q$ cm^{-1} at the entrance pinhole. In 0.6-Torr Xe, the dispersion of the target gas was estimated to be 1.19 cm^{-1} for the 11th harmonic, 1.15 cm^{-1} for the 13th harmonic, 1.14 cm^{-1} for the 15th harmonic, 1.15 cm^{-1} for the 17th harmonic, and 1.18 cm^{-1} for the 19th harmonic. Considering only the geometrical phase and gas dispersion in the neutral atom, phase matching cannot always be satisfied perfectly because the Gouy phase changes along the propagation distance. On the other hand, the absorption-limited conditions [15] for medium, coherence, and absorption lengths are given by $L_{\mathrm{med}}>3L_{\mathrm{abs}}$ and $L_{\mathrm{coh}}>5L_{\mathrm{abs}}$. The absorption length for 0.6-Torr Xe was estimated to be 1.35 cm for the 11th, 1.58 cm for the 13th, 1.89 cm for the 15th, 3.65 cm for the 17th, and 4.3 cm for the 19th harmonic. Although a shorter absorption length is actually worse for the generation process, we have obtained a higher energy for the 11th harmonic than those for the 15–19th harmonics. This is explained by considering the difference in atomic polarizabilities in this range of harmonics. As the 11th harmonic is only marginally in the plateau, it should be expected that it has a larger polarizability. In the phase-matched process, the 11th to 15th order harmonics satisfied the absorption limited HHG condition in 0.6-Torr Xe.

Emission angles (mrad) can be converted to the spatial profile of the harmonic by considering the distance between the harmonic source and the spectrometer slit. The output beam divergence of the 13th order harmonic was measured to be ~0.5 mrad (FWHM) with a Gaussian-like profile.

Figure 1(c) shows a typical harmonic spectrum for $L_{\mathrm{int}}=10$ cm and 1.8-Torr Ar. The pump pulse energy and the truncated diameter were set at 20 mJ and 18 mm, respectively. As is shown in the figure, second-order diffraction was observed around the 11th and 13th harmonics, and low-order harmonics (<21st) are not phase matched under this condition and are strongly absorbed in Ar. Here, it must be noted that the relative diffraction efficiency of a flat-field normal-incidence XUV spectrometer becomes the maximum at 60 nm. Since the efficiency gradually decreases for shorter wavelengths, the maximum harmonic intensity was obtained at the 27th order harmonic. The absorption length L_{abs} for 1.8-Torr argon gas was calculated to be 1.16 cm for the 23rd, 2.39 cm for the 25th, and 6.81 cm for the 27th harmonic. The 23rd and 25th order harmonics satisfied the absorption limited conditions, therefore, those orders were saturated under our experimental conditions. On the other hand, the 27th order harmonic did not satisfy the conditions, because of low absorption. Under the optimized condition, the beam divergence of the 27th harmonic was measured to be 0.7 mrad with a Gaussian-like profile.

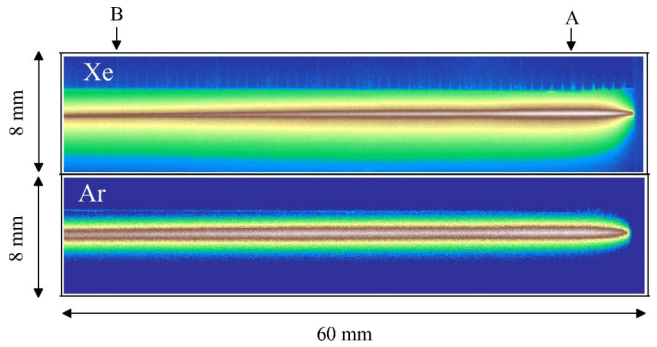

FIG. 2. (Color online) 2D plasma fluorescence in Ar and Xe gases. Spatial resolution of the measurement optical system was estimated to be 200 μm.

A typical 2D-plasma column image obtained under the experimental conditions shown in Fig. 1 is shown in Fig. 2. This image was taken using a wide-angle optical system, and the spatial resolution was estimated to be 200 μm. Top and bottom figures correspond to Xe and Ar gas cases, and the horizontal and vertical axes correspond to the z and y spaces, respectively. The pump pulse propagated along the right to left direction, and the entrance pinhole was located at the right-hand end. In the Ar case, the fluorescence intensity was almost constant along the propagation coordinate. On the other hand, in the Xe case, the fluorescence intensity became maximum at the entrance pinhole, and gradually decreased along the propagation coordinate. In addition, we found a remarkable structure similar to a plasma channel at the central part in the Xe gas case. The detailed results are shown in the following section.

D. Relation of HH and plasma column structure

To investigate the relationship between the harmonic output signal and the plasma column structure, we measured HH intensity and plasma fluorescence under the same experimental conditions. In these experiments, we chose the target gas pressure, focusing position, and input laser energy as variable parameters. The focusing geometry and the target gas position relative to the focusing point, as well as their

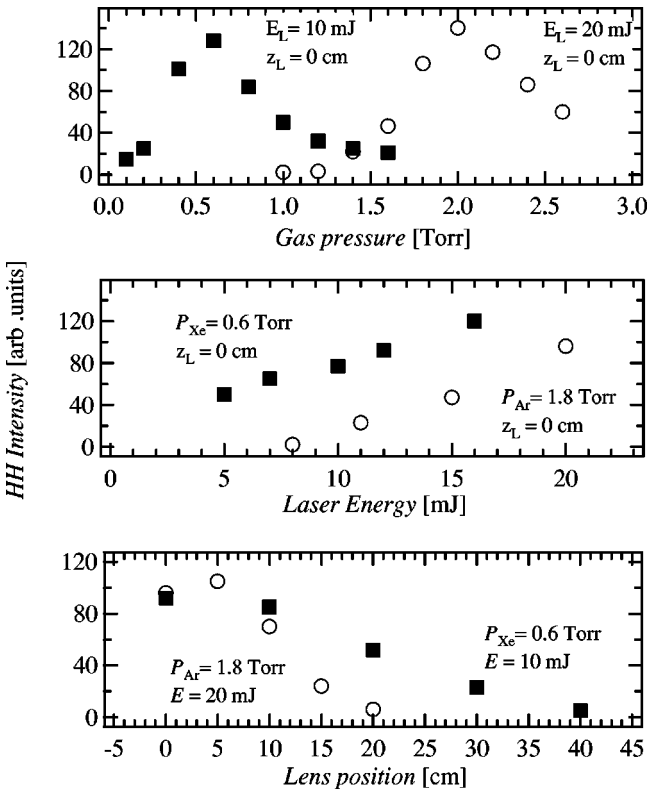

FIG. 3. HH intensity as a function of gas pressure (top panel), input laser energy (middle panel), and lens position (bottom panel). Open circles and solid squares correspond to the 13th HH in Xe and the 27th HH in Ar, respectively. P, Z_L, and E_L correspond to target gas pressure, focusing lens position, and input laser energy, respectively. Inset figures indicate other experimental conditions for each case, except for the changing parameter.

influence on the phase matching, have been key issues in HHG optimization, as the interaction intensity at the medium dictates the propagation condition of the pump pulse. In addition, the phase matching of HHG is influenced by target gas pressure. Here, we define $z_L=0$ when the focusing point of the pump pulse is at the entrance pinhole, i.e., the cell is placed on the diverging beam. At positive z_L values, the interaction cell is placed in the diverging beam, i.e., with the entrance pinhole after the focus. In this experiment, the medium length was fixed to be 10 cm for both gases, since the signal of the 13th and 27th harmonics saturated at 10-cm length [9]. First, we show the HH signal results, and second we show the measurement results of the plasma column structure.

Figure 3 shows the dependence of the HH output signal on the variable parameters. Open circles and solid squares correspond to the 13th HH in Xe and the 27th HH in Ar, respectively. The top panel describes the gas pressure dependence of the HH signal, while other parameters were kept fixed. The maximal HH intensities were obtained for a Xe gas pressure of 0.6 Torr for 13th HH and an Ar gas pressure of 2.0 Torr for 27th HH. Also, the optimized gas pressure for each case had a finite tuning range. This finite range was explained [10] by the phase-matching condition and target gas absorption. Since the dispersion of Xe for the 13th HH is larger than that of Ar for the 27th HH, the optimized gas pressure of Xe becomes small compared to that of Ar. In addition, at gas pressures higher than the optimal gas condition, HH is decreased by absorption due to neutral atoms.

The middle and bottom panels in Fig. 3 show the laser energy and focus position dependence of the HH signal, respectively. The input laser energy was varied by changing the amplifier timing of the yttrium aluminum garnet (YAG) laser which pumps the final amplifier in the laser system; the focusing position was controlled by moving the focusing lens along the propagation axis of the pump pulse. In Xe gas, the HH intensity increased with increasing the pump pulse energy up to 16 mJ. When a higher energy was used, the harmonic energy was decreased. Similarly, the 27th HH in Ar increased with increasing the pump pulse energy. However, since the frequency spectrum of the pump laser pulse was modulated by the self-phase modulation (SPM) at the entrance window (CaF_2), we could use only $\sim$20 mJ in this experimental setup. When we increased the input energy above 20 mJ, we could obtain neither good spatial quality nor high energy within the observed spectral region. Therefore, the pump energy was set at 20 mJ. Presented in the bottom panel is the dependence of HH intensity on z_L. The harmonic signal gradually increased toward the entrance pinhole, and the maximal harmonic signal was obtained around $z_L=0$ for both gas cases. The 27th HH in Ar had a narrower distribution than the 13th HH in Xe, because the interaction intensity necessary to generate a higher harmonic has a narrower distribution along the z_L coordinate. Indeed, as seen from the energy dependence of the HH signal, the slope for Ar is larger than that for Xe (see middle panel of Fig. 3).

The absolute output energy of HH was measured using an XUV photodiode. This photodiode was inserted in front of the spectrometer, and the output signal was recorded directly on an oscilloscope. A thin aluminum filter (0.2μm) was placed between the sources and the detector to eliminate the pump pulse and pass only the 11th through 45th harmonics (17 to 70 eV). The maximal harmonic energy under the optimized conditions of the 13th and the 27th HH attained 4.7 μJ and 0.32 μJ, respectively.

As mentioned before, during HHG experiments, the plasma fluorescence was also observed by use of a CCD camera (see Fig. 2). Figures 4 and 5 show the one-dimensional (1D) plasma fluorescence distribution along the propagation coordinate. This distribution was obtained by image integration along the vertical axis in Fig. 2. To compare the intensity distribution structure, the fluorescence intensities were normalized to the maximum signal. In both Figs. 4 and 5, panels from (a) to (c) correspond to gas pressure, input laser energy, and focus point dependence, respectively. The other parameters are the same as in Fig. 3. The pump pulse propagated from right to left.

In the Ar gas case, the intensity distribution did not depend on the target pressure [see Fig. 4(a)]. Note that this is normalized intensity; the real intensity is maximum at $P_{Ar}=2.6$ Torr. In the same way, when we changed the input laser energy, the distribution had almost the same form. On the other hand, the distribution had a strong dependence on the focusing point [see Fig. 4(c)]. Upon moving the lens away

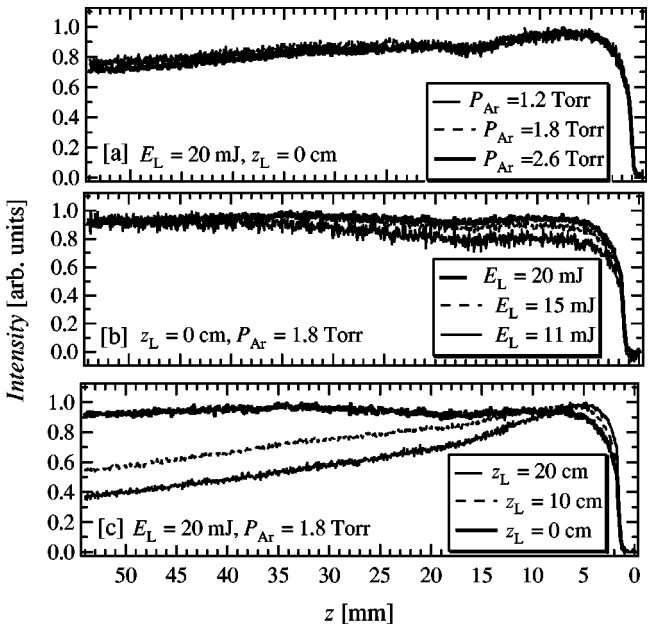

FIG. 4. Measured 1D Ar plasma fluorescence with 200-shots accumulation under several HHG conditions. (a) is gas pressure dependence, (b) is laser energy dependence, and (c) is lens position dependence. Inset figures indicate other experimental conditions, except for the changing parameter.

from the interaction cell, i.e., with the entrance pinhole after the focus, the intensity distribution rapidly decreased from the input towards the output pinhole. Under the HH optimization condition (E_L=20 mJ, z_L=0 cm, P_{Ar}=1.8 Torr), the plasma fluorescence along the propagation coordinate exhibits a flat distribution.

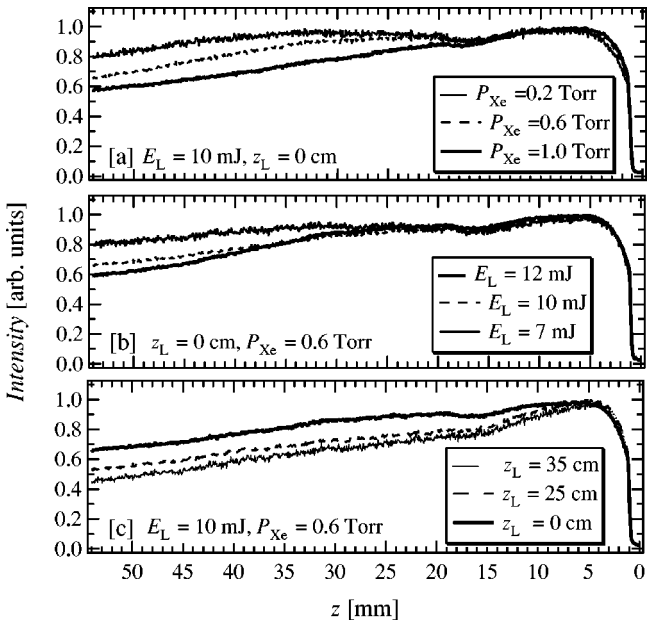

FIG. 5. Measured 1D Xe plasma fluorescence with 200-shots accumulation under several HHG conditions. (a) is gas pressure dependence, (b) is laser energy dependence, and (c) is lens position dependence. Inset figures indicate other experimental conditions, except for the changing parameter.

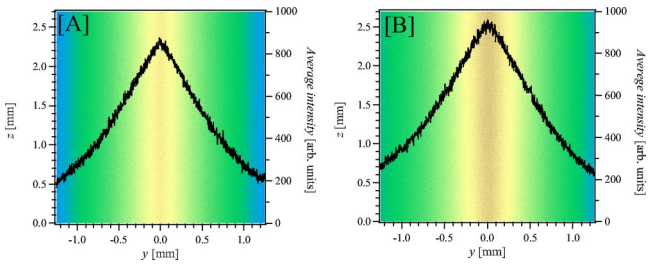

FIG. 6. (Color online) Ar plasma fluorescence with 500-shots accumulation measured by use of high-resolution optical system. HHG conditions were optimized with E_L=20 mJ, P_{Ar}=1.8 Torr, and the lens position was set at 0 cm. (a) and (b) correspond to z=5 mm and z=50 mm, respectively [see Fig. 2 in the (a) and (b) positions].

For the Xe gas case in Fig. 5, the plasma fluorescence intensity distribution changed at each condition. Upon increasing the target gas pressure, the intensity distribution became flat [see Fig. 5(a)]; however, the real intensity decreased with increasing the gas pressure. Also, at increased input laser energy [see Fig. 5(b)], the intensity along the propagation coordinate decreased more than that at low input laser energy. Moving the lens away from the interaction cell, i.e., with the entrance pinhole after the focus, the intensity distribution gradually decreased from the input towards the output pinhole, and the real fluorescence intensity decreased. However, the intensity decreasing ratio between z=0 to 55 mm became smaller than that in the Ar case. Note that for Xe, the lens excursion was larger than that for the Ar case. For the time being, we note that under the HH optimization condition (E_L=16 mJ, z_L=0 cm, P_{Xe}=0.6 Torr), the plasma fluorescence along the propagation coordinate was different to that in the optimized Ar case.

As the next step, we investigated the detailed structure of plasma fluorescence in the transverse coordinate. In this measurement, we used an optical system with high spatial resolution, which was estimated to be $\sim$15 μm. To investigate the structure of the plasma column, we measured it at two points along the propagation coordinate. One is at 5 mm after the entrance pinhole, which corresponds to the starting point of pump propagation (labeled A in Fig. 2). The other is at 50 mm after the entrance pinhole which corresponds to the middle of the medium length (labeled B in Fig. 2).

Figure 6 shows the transverse profile of the Ar plasma column under the optimized HHG condition. The propagation coordinate of pump pulse corresponds to the left vertical axis in Fig. 6, and the horizontal axis y denotes the transverse coordinate. The solid line shows the transverse profile integrated for a slice of 2 mm along the propagation coordinate z. The fine structure of the Ar plasma column shows the same profile at both A and B observation points. This structure was the same under all experimental conditions, such as target gas pressure, input laser energy, and focusing point of pump pulse.

The transverse structure of the Xe plasma column under the optimized HHG condition is shown in Fig. 7. As is obvious from Fig. 7, the structure is different from that observed in the Ar case. In particular, we found a remarkable

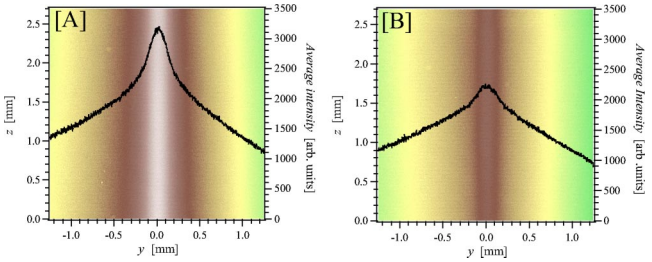

FIG. 7. (Color online) Xe plasma fluorescence with 200-shots accumulation measured by use of high-resolution optical system. HHG conditions were optimized with $E_L=10$ mJ, $P_{Xe}=0.6$ Torr, and the lens position was set at 0 cm. (a) and (b) correspond to $z=5$ mm and $z=50$ mm, respectively [see Fig. 2 in (a) and (b) positions].

column structure at the central part ($|y|<0.3$ mm). To understand this structure of the Xe plasma column, we investigated its dependence on the focusing point position, which corresponds to the data in Fig. 5(c). Note that the gas pressure and input energy were not changed. Figure 8 depicts the Xe fluorescence transverse profiles at $z=5$ mm, and Fig. 9 shows the same data for $z=50$ mm. From top to bottom in the figure correspond to the focusing point of the pump pulse at $z_L=0$, 15, 25, and 35 cm. Thin dotted lines indicate the experimental result, and dashed lines indicate the calculation results, which will be discussed later. When the focusing point was located at $z_L=0$, the profile was Gaussian-like for $|y|<2.5$ mm and $z=5$ mm (see top profile in Fig. 8), and the intensity gradually decreased along the y coordinate. On the other hand, at the $z=50$ mm point (see the two top profiles in Fig. 9), the transverse profile exhibits a central top-hat shape. With moving the focus away from the entrance pinhole, we obtained the data plotted from top to bottom in Figs. 8 and 9. One can note that the central top-hat shape in Fig. 8 gradually disappears as z_L increases. In addition, one basic item of information which we required, the time dependence of the fluorescence signal, was measured for Xe by

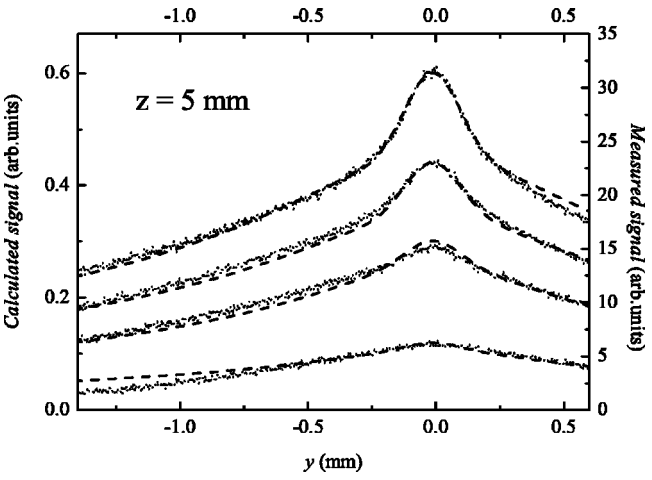

FIG. 8. Calculated (dashed lines) and experimental (thin dotted lines) fluorescence radial profiles for Xe and $z=5$ mm. From top to bottom, the pairs of curves correspond to $z_L=0$, 15, 25, and 35 cm, respectively.

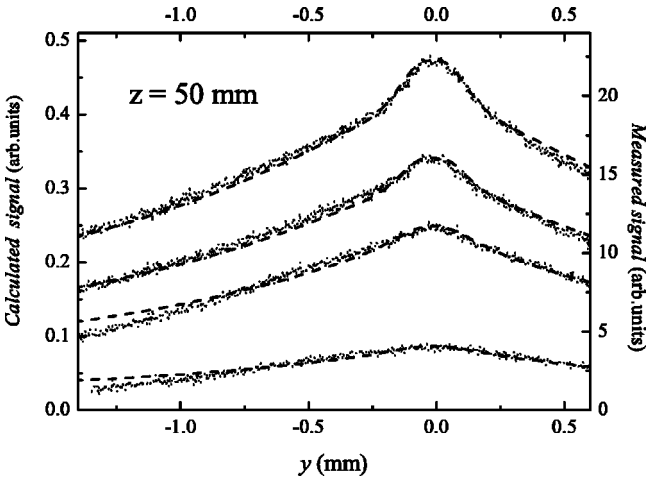

FIG. 9. Calculated (dashed lines) and experimental (thin dotted lines) fluorescence transverse profiles for Xe and $z=50$ mm. From top to bottom, the pairs of curves correspond to $z_L=0$, 15, 25, and 35 cm, respectively.

using a fast photodiode and a BG40 filter which is transparent in the 300–700 nm spectral region. The measured signal shows a main spike of about 25-nsec FWHM, followed by a slower decrease with a time constant of about 150 nsec. For 0.6 Torr, the amplitude of the first peak is about eight times higher than the amplitude of the decreasing part. Our fluorescence signal was measured as an average over time spans much longer (microseconds) than the plasma fluorescence time.

E. Discussion and summary of experimental results

We summarize the experimental results of HHG and plasma column structure in this section. On the basis of the experimental results, we also denote the object of our numerical calculation.

The experimental optimized HH energy scaling parameters for Ar and Xe gas are listed in Table I. As was shown in Fig. 3, the HH output signal in the case of both gases reached a maximum at the $z_L=0$ focusing point. Close to the optimized condition, we measured the transverse fluorescence structure in Xe. The central part of this structure was Gaussian-like at the $z=5$ mm point, and was modified to form a top-hat shape at the $z=50$ mm point.

Under the $z_L=0$ condition, the geometrical focus intensity in vacuum was estimated to be more than 10^{15} (W/cm^2) from the spot size of the pump pulse. This focusing intensity

TABLE I. Typical experimental optimization conditions and output harmonic energies.

Target gas	Ar_{27th}	Xe_{13th}
Focusing length (mm)	5000	5000
Pump energy (mJ)	20	16
Medium length (cm)	10	14
Target gas pressure (Torr)	1.8	0.6
Harmonic energy (μJ)	0.32	4.7

will break the phase-matching condition using a neutral atom. On the other hand, by using the relation $h\nu = I_p + 3.17U_p$, we estimated the effective interaction intensity of the pump pulse. Here, I_p is the atom ionization potential, and U_p is the electron quiver energy, which is given by $U_p = 9.3\times 10^{-14} I_0\ (\mathrm{W/cm^2})\lambda_0^2\ (\mu\mathrm{m})$. From the observed Ar HHG spectral distribution in Fig. 1, the interaction intensity was estimated to be $\sim 1\times 10^{14}\ (\mathrm{W/cm^2})$. From the Ammosov-Delone-Krainov (ADK) model [18], the ionization probability was estimated to be less than 1% at $1\times 10^{14}\ (\mathrm{W/cm^2})$. This low ionization is supported by the increase of the 27th harmonic energy, in which phase matching is satisfied in the nonionized condition. The almost perfect Gaussian profile of the HH also suggests that there is no density disturbance due to ionization in the interaction region.

To clarify the relationship between HHG and pump propagation, we conducted a numerical calculation of the propagation dynamics of intense femtosecond laser pulses in Ar and Xe. In the following section, we show the numerical model used for the pulse propagation and the model developed to model the fluorescence intensity data. The results are presented and discussed in Sec. IV.

III. NUMERICAL MODEL

For the calculation of the fundamental field in the interaction region, we basically adopted a nonadiabatic 3D model used [17] to study the pulse propagation in the few optical cycle regime. Ionization is the main contribution, but also dispersion and Kerr terms were considered in the refraction index calculation, as described below. We also describe the models used for Xe and Ar ionization. To calculate the transverse profile of the fluorescence we developed a model in which electron expansion after the laser pulse is considered.

A. Propagation of the fundamental field

In an ionized gas, pulse propagation is affected by diffraction, refraction, nonlinear self-focusing, ionization, and plasma defocusing. The pulse evolution in such a medium is described by the wave equation which can be written as [19]

$$\nabla^2 E_1 - \frac{1}{c^2}\frac{\partial^2 E_1}{\partial t^2} = \frac{\omega^2}{c^2}(1-\eta_{eff}^2)E_1, \tag{1}$$

where $E_1 = E_1(r,z,t)$ is the transverse electric field of the laser, of frequency ω. Axial symmetry is assumed, therefore cylindrical coordinates are used throughout. The effective refractive index of the medium can be written as

$$\eta_{eff}(r,z,t) = \eta_0(r,z,t) + \eta_2 I(r,z,t) - \frac{\omega_p^2(r,z,t)}{2\omega^2}. \tag{2}$$

The first linear term $\eta_0 = 1 + \delta_1 - i\beta_1$ accounts for the refraction (δ_1) and absorption (β_1) while the second term accounts for the optical Kerr nonlinearity depending on laser intensity I. Finally, the third term contains the plasma frequency $\omega_p = (4\pi e^2 n_e/m)^{1/2}$ and accounts for the presence of a density n_e of electrons (of mass m and charge e) per unit volume. Keeping, at this stage, only the real terms in the refractive index, Eq. (1) becomes

$$\nabla^2 E_1 - \frac{1}{c^2}\frac{\partial^2 E_1}{\partial t^2} = k^2\left(\frac{\omega_p^2}{\omega^2} - 2(\delta_1 + \eta_2 I)\right)E_1. \tag{3}$$

The method adopted to solve Eq. (1) is described by Priori *et al.* [17] and will only briefly be mentioned here. We write the equation in the moving frame, and, after performing the paraxial approximation, eliminate the temporal derivative by a Fourier transform, and obtain the equation

$$\nabla^2 \tilde{E}_1 - \frac{2i\omega}{c}\frac{\partial \tilde{E}_1}{\partial z} = F_T\left[k^2 E_1\left(\frac{\omega_p^2}{\omega^2} - 2(\delta_1 + \eta_2 I)\right)\right], \tag{4}$$

where F_T is the Fourier-transform operator acting on the temporal coordinate and $\tilde{E}_1(r,z,\omega) = F_T[E_1(r,z,t)]$. We mention that Eq. (4) is solved taking into account only the electrons plasma term. From the numerical point of view, the right-hand side of Eq. (4) has both an implicit (through plasma frequency term and $\eta_2 I$ term) and an explicit dependence on E_1. For this reason it was solved self-consistently in every δz step as follows. After advancing the solution $E(r,z,\omega)$ by a Crank-Nicolson scheme, we calculated $E(r,z,t)$ by the inverse Fourier transform, then we evaluated again the right-hand term of Eq. (4), first in the t domain and then in the ω domain. The Crank-Nicolson scheme was applied again on the same step δz and a new $E(r,z,\omega)$ solution was obtained. The iteration was repeated until the difference between the new and old solutions was under an imposed threshold.

The imaginary part of the refractive index was also considered in order to estimate the damping of the wave during propagation. We assume that the energy lost by the pulse is solely due to having to supply energy for ionization. To find this contribution we proceed as in Ref. [20], by writing the energy balance for the ionization process: the energy lost by the pulse between z and $z+\delta z$ is the opposite of the energy gained by the electrons in the same interval. One obtains the imaginary contribution to the refractive index as $\gamma = (n_0 I_p w\lambda)/4\pi I$, where n_0 is the atomic density, I_p the ionization potential, and w the ionization rate for an average intensity I. The energy loss was estimated for each (r,z) point after every successful integration step, and the dumped field was used in the next integration step. In general, this quantity is small: for the highest ionization case considered here, we obtained a loss of energy by ionization of 1.1%.

To start the calculations we used the *measured* energy E_{pulse} and duration τ_p of the pulse to calculate the peak intensity, $I_0 = 2E_{pulse}/(\pi w_0^2 \tau_p)$. A Gaussian distribution in time and space was considered for the laser beam; the beam waist was approximated as $w_0 = f\lambda/D$, where D is the diameter of the iris used to truncate the beam before focussing. By placing the interaction cell in a specific z_L position, the E_1 initial and boundary values, needed to start solving the propagation equation, were calculated. In order to avoid re-

flection effects from the boundaries, we set the integration region radius to be four times larger than the beam waist.

B. Ionization model

The ionization of rare-gas atoms in a high-intensity laser field is a complex and computationally demanding problem. It is not the goal of our study, but choosing an appropriate yet computationally simple model for ionization is important for a realistic description of ultrashort pulse propagation.

For the calculation of the Xe ionization rate, a mixed model was adopted. The intensities generated under our experimental conditions range from 10^{13} W/cm^2 to about 2.5 $\times 10^{14}$ W/cm^2. Depending on the laser intensity, the creation of free electrons can be described by one of the following models: tunneling or multiphoton ionization (MPI). The separation between these regimes is given by the Keldish parameter $\gamma_K=\sqrt{2I_p/U_p}$, where $U_p=E^2/4\omega^2$ is the ponderomotive energy. For $\gamma_K<1$, the tunnelling regime is dominant and the ionization rate $w(t)$ can be well described by the ADK formula [18]. In atomic units it can be written as

$$w(t)=I_p C_{n*}^2\left(\frac{4I_p}{\Omega_t}\right)^{2n^*-3/2}\exp\left(-\frac{4I_p}{3\Omega_t}\right), \tag{5}$$

with

$$C_{n*}^2=\frac{2^{2n^*}}{n^*\Gamma(n^*+1)\Gamma(n^*)}, \tag{6}$$

being a constant depending on the Γ Euler function and

$$\Omega_t=\frac{|E(t)|}{\sqrt{2I_p}},\quad n^*=Z(I_{ph}/I_p), \tag{7}$$

where Z is the net resulting charge of the ion ($Z=1$ in our case) and I_p and I_{ph} are the ionization potentials of Xe and hydrogen atoms, respectively.

For $\gamma_K>1$, the multiphoton regime is the strongest effect and the rates were used as calculated by Kulander [21] for the valence p shell of Xe. As the calculated MPI rates are given in Ref. [21] for 293 nm, 586 nm, and 1064 nm, an interpolation was carried out to find the rates for 800 nm. We mention that, for γ_K close to unity, the ADK and MPI rates have closed values so that a smooth rate dependence on laser intensity was obtained.

Ultrafast ionization rates of Ar were recently measured [22] using a pump-probe technique. The ionization rates reported were used to build up an interpolating polynomial from which the rates for a given instantaneous intensity could easily be calculated. The resulting rate values were found to be smaller but close to the ADK rates corrected for intensity with a 1.7 factor, as described by Augst *et al.* [23].

C. Modeling fluorescence

In modeling the fluorescence signal which we measured, the basic assumption we make is that the observed fluorescence originates from the ions, thus, its intensity is proportional to the local ion concentration. In addition, we assumed that the ion concentration is equal to the electron concentration $n_e(r,z,\tau_p)$ at the end of the laser pulse. These assumptions are true only if we neglect multiple (mainly double) ionization processes in the interaction region and assume full ionization efficiency in the electron-atom collisions. The agreement with experimental data suggests that, for a qualitative description of the fluorescence, the above assumptions can be made in our experimental conditions.

As mentioned before, to obtain the fluorescence profiles along the propagation direction, the measured data were integrated in the transverse direction. As a result, the fluorescence signal $S(z)$ can be linked to the radially integrated electron concentration,

$$S(z)\sim\int n_e(r,z,\tau_p)rdr, \tag{8}$$

over the interaction region. An unknown parameter is the gas distribution in the vicinity of the two pinholes, but it will only influence the fluorescence signal for about 5 mm after the input pinhole. On no physical grounds but solely to fit the data, we used the rational function $y=1.1x/(0.1+x)$, with x in mm, to describe the gas distribution for this region. For the rest of the cell the density was assumed to be constant.

The transverse profiles of the fluorescence were measured over a $\Delta z=2$ mm thin region, and therefore we can relate them to the radial profiles of the electron concentration. One basic item of information which we required, the time dependence of the fluorescence signal, was measured for Xe by using a fast photodiode and a BG40 filter which transmits in the 300–700 nm spectral region. The measured signal shows a main spike of about 25-nsec FWHM, followed by a slower decrease with a time constant of about 150 nsec. For 0.6 Torr, the amplitude of the first peak is about eight times higher than the amplitude of the decreasing part. With increasing pressure the slow decreasing part gains amplitude relative to the spike. It is therefore reasonable to assume that the spike is due to radiative transitions between the excited levels of the ions, while the slower decreasing part is fluorescence induced by electron-atom or electron-ion collisions during electron expansion out of the interaction region. Our fluorescence signal was measured as an average over time spans much longer (microseconds) than the plasma fluorescence time span. Therefore, the electron expansion had to be taken into consideration and was described by a 1D advection-diffusion equation,

$$\frac{\partial n}{\partial t}+\frac{\partial(nv)}{\partial y}-\frac{\partial}{\partial y}\left(D\frac{\partial n}{\partial y}\right)=0, \tag{9}$$

where D is the diffusion coefficient of the electrons, of density n, in the neutral atoms, and v is the velocity with which electrons expand from the interaction region. The equation was solved numerically by assuming initial conditions similar to the electron density distribution created by the laser pulse. This distribution could be obtained by solving the propagation equation for the laser field. At every integration step, the solution $n(y,t)$ of Eq. (5) was weighted by the

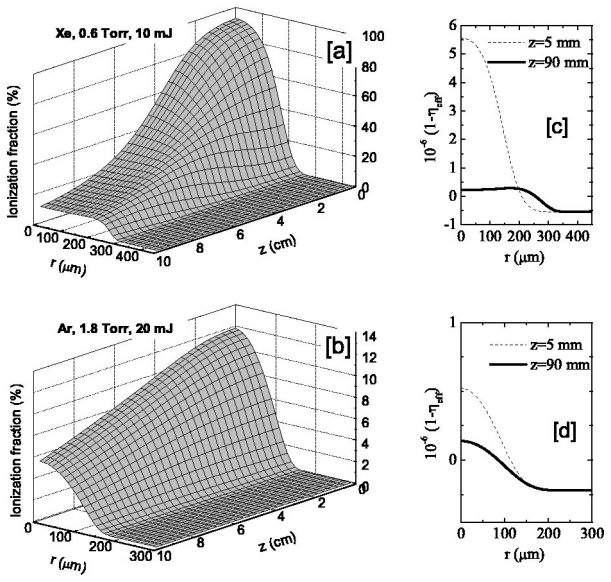

FIG. 10. Calculated ionization fraction in the interaction region for Xe (a) and Ar (b). Panels (c) and (d) show the radial profiles of the quantity $(1-\eta_{eff})\times 10^{-6}$ at $z=5$ mm (dashed lines) and $z=90$ mm (solid lines) for Xe and Ar, respectively. Cell position $z_L=0$ in both cases.

fluorescence intensity $I_f(t)$ and was eventually used to calculate the fluorescence signal $S(y)$ as

$$S(y)\sim \int n(y,t)I_f(t)dt. \tag{10}$$

The parameters of the model are the diffusion constant D, the velocity v, and the initial electron distribution in the interaction region. In fitting the experimental data obtained for different experimental conditions, these parameters were adjusted so as to obtain a best fit between the measured transverse profile and $S(y)$. Conventionally one should solve Eq. (5) in cylindrical coordinates and perform an additional averaging to transform the radial profiles into transverse profiles in order to compare with experimental data. Solving Eq. (5) in Cartesian coordinates without averaging is an approximation that may affect the values of D and v but not their qualitative dependence on experimental conditions. The time step was chosen to be sufficiently small (10 ps) to ensure the independence of the results from this parameter. The integration region was chosen to be sufficiently large (25 mm) that the boundary conditions would not influence the calculated solution.

IV. RESULTS OF NUMERICAL SIMULATION

In the beginning of this section, we show some results obtained by solving Eq. (1), as these results help us to explain the fluorescence profiles. For two typical cases for Xe and Ar we demonstrate that the solution of the propagation equation presents, in the case of Xe, a channeled structure, even in the absence of Kerr nonlinearity. For Ar this structure did not occur. As we saw in the experimental section, the fluorescence profiles, both in the axial and in the transverse direction, appear different in the two cases.

The calculated electron densities are shown in Fig. 10 for the two typical cases studied for Xe (a) and Ar (b). The position of the 10-cm cell is the same in both cases, namely, $z_L=0$. The 10-mJ pulse induces an almost full ionization in Xe and the initial ionization profile, and following the initial laser intensity profile, transforms gradually into a channel-like profile, with an almost flat central profile, and a sharp decrease at about 250 μm. In the channeling region the field intensity keeps fairly constant. On the other hand, the 20-mJ pulse in Ar induces a lower fraction of ionization, and the initial defocusing continues along the propagation and produces a continuous decrease in the laser intensity.

Usually, channeling occurs [19] when a balance between Kerr self-focusing and electron defocusing takes place. However, in our range of pressures and field intensities, the Kerr contribution to the refractive index is small compared to that given by the electrons. Therefore, it seems unlikely that the ionization nonlinearity alone, without any focusing nonlinearity, can be a sufficient mechanism for guiding of an ultrashort laser pulse. However, the data in Fig. 10(a) suggest that the ionization profile formed initially is able to drive the formation of a channeled structure. On the other hand, the case shown Fig. 10(b), where the channel is not formed, suggests that the initial electron concentration must reach a certain threshold in order to lead to the channel formation. In both cases, the electron plasma acts as a diverging lens with decreasing focal power as r increases. The initial laser wave front will change its radius of curvature more in the central and less in the peripheral regions. In particular, this radius of curvature becomes infinite when [24] the change of the index of refraction in the radial direction verifies the equation

$$\delta\eta_{eff}=\frac{\lambda^2}{2\pi^2 w_0^2}, \tag{11}$$

where w_0 is the waist size of the laser beam and λ is the wavelength. For both our cases the geometrical factor is $\lambda^2/2\pi^2 w_0^2=0.65\times 10^{-6}$ for $w_0=230$ μm. From the data for Xe in Fig. 10(c), it results that, at $z=5$ mm, the $\delta\eta_{eff}$ increment required by Eq. (11) is satisfied for a radius of around 200 μm. For an index change in excess of that given by Eq. (11), the laser intensity decreases due to an increased divergence from the plasma lens. This gradually decreases the ionization level down to a self-regulated level. For $z=90$ mm [see Fig. 10(c)] this self-regulated regime is reached and one can see that the increment in the refractive index verifies Eq. (11). As was earlier anticipated by Rankin *et al.* [24], and later confirmed by computer calculations [25–27], such a distribution of the refractive index can guide an electromagnetic wave in the form of a leaking mode with exponentially small losses over distances of many free Rayleigh lengths. This regime of guiding can be seen in Fig. 10(a).

For Ar, the situation is different: at $z=5$ mm [see Fig. 10(d)] the variation of the refractive index is much smaller than it is in Xe. As one can see, Eq. (11) is fulfilled for a radius of 20–30 μm which is too small to generate a self-

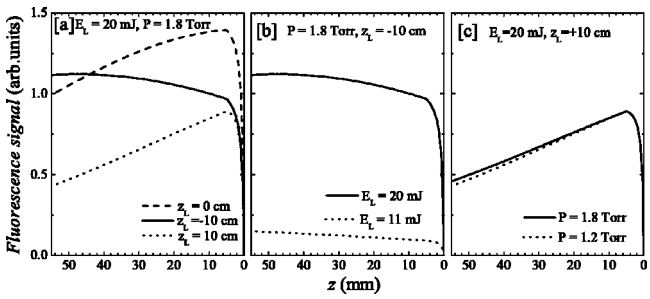

FIG. 11. Calculated fluorescence axial profiles for Ar. Parameters of the calculations are specified for each case.

guided structure. As a result, the intensity continuously decreases and no top-hat configuration is observed in the central part of the beam.

The fluorescence profiles along the propagation direction, calculated for Xe, are presented in Fig. 12. The parameters used for calculations, pulse energy and duration, cell position with respect to the focus, and gas pressure are identical with the experimental conditions.

As is evident from Fig. 12, the agreement with the measured intensities in Fig. 5 is very good; the slight differences concerning the slope of the curves could be attributed to the ionization model used or to the uncertainities connected with the cell position with respect to the focus.

In Fig. 11 we present similar data for Ar. Again the experimental data were used as input parameters in the calculations. However, in this case we could find agreement with the experimental data in Fig. 4 only after assuming a 10-cm shift in the cell position, namely, assuming the $z_L=-10$, 0, and 10 cm, instead of the measured positions $z_L=0$, 10, and 20 cm, respectively. The amplitudes of the fluorescence intensities in the three cases, with the highest amplitude for the assumed $z_L=0$, also support this shift. The disagreement is, however, tolerable, because under our loose focusing geometry, with a Rayleigh length around 21 cm, an uncertainity of up to several centimeters in the cell position is quite possible. On the other hand, the cell position is determined in air using low energy pulses. The entrance window might have an influence on the focus position, as the pulse energy increases. Indeed, for Ar we used higher energy pulses than for Xe, which might have a greater influence on the focus position.

We note that the ratios between the calculated intensities for different working conditions were also found to be in

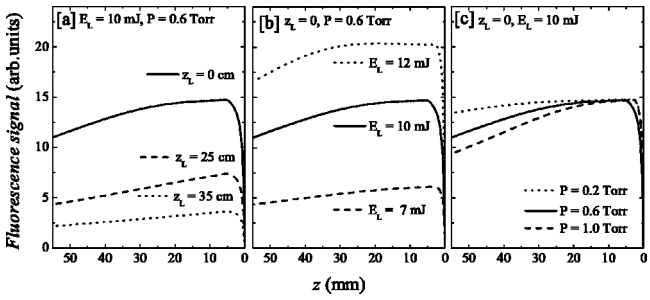

FIG. 12. Calculated fluorescence axial profiles for Xe. Parameters of the calculations are specified for each case.

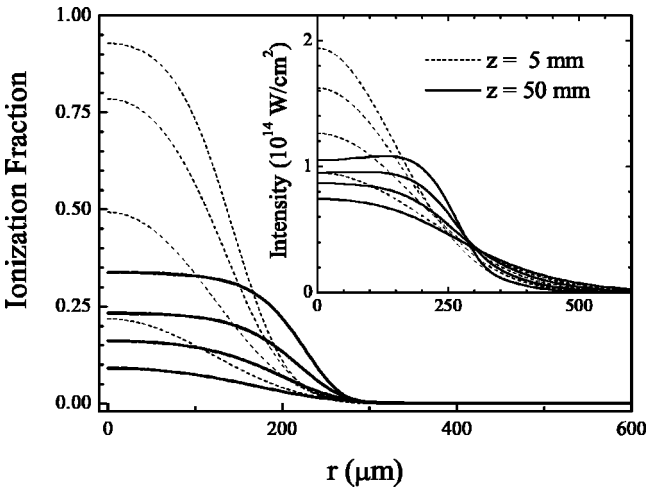

FIG. 13. Calculated radial profiles for the ionization fraction and intensities (in the inset) for $z=5$ and $z=50$ mm, with Xe, 0.6 Torr, 10 mJ. From top to bottom, the families of curves correspond to $z_L=0$, 15, 25, and 35 cm, respectively.

reasonable agreement with the corresponding experimental values.

For Ar, the axial distributions of the fluorescence only slightly deviate from what a Gaussian distribution of the field would create for the same cell position. As the scale unit is the same in Fig. 12 and Fig. 11, we can see that the intensities are around one order of magnitude lower for Ar, thus, there is a much lower electron density.

The Xe fluorescence data, both axial and transverse, exhibit different features because they originate from from a field configuration under channeling condition. To discuss these data further we refer to Fig. 13 where we plotted, for $z=5$ mm and $z=50$ mm, the calculated radial dependence of the ionization fraction and intensity for Xe. From this figure, we see that, for $z_L=25$ and $z_L=35$ cm, the channel formation is less evident. For $z_L=35$ cm, neither the electron nor the field intensity exhibit top-hat radial profiles at $z=50$ mm. This is mainly because the intensity at the input pinhole is too low to generate the required refractive index variation. In the $z_L=0$ case, this top-hat profile is clearly seen in both the radial distributions in Fig. 13.

In Fig. 13 we also see that, regardless of the input pinhole position, the intensity in the channel clamps to a self-regulated value which is decreased only slightly by increasing z_L and thus by decreasing initial intensity. However, the change in fluorescence intensity, as seen from Fig. 12(a), seems stronger. One explanation is the nonlinear dependence of the ionization yield on intensity. Another effect, acting in the same direction, is a higher channel radius for a higher incident intensity. The higher the incident intensity, the higher the radius for which Eq. (11) is verified. This effect will also affect the harmonic field intensity, as we will see further.

The data in Fig. 12(b) can be explained in the same terms: as input energy increases, both the increase of the intensity in the channel and the increase of the channel radius will cause an increase in the total fluorescence signal. However, we mention that, as seen also from the experimental data in Fig.

5, the higher the input energy, the faster the decrease of the fluorescence along the propagation direction. This implies a faster channel degradation which will limit the harmonic phase matching, and thus the conversion efficiency.

The results in Fig. 12(c), for different gas pressures, can be explained by analyzing the computed results for the electron density. At 0.2 Torr, the channel is not formed, and the electron density configuration is similar to that in Fig. 10(b). Comparing the 0.6-Torr and 1.0-Torr cases, where channeled structures occur, the computed result shows that the higher the gas pressure the lower the electron concentration. The required refractive index increment, such as that satisfying Eq. (11), is the same in both cases, however, outside the channel the refractive index will be higher for higher pressures, as it is proportional to the density of neutrals. The fluorescence will be therefore less intense for higher pressures, as shown in Fig. 12(c).

The features of the channeled propagation were further analyzed by modeling the transversal profiles for the case of Xe. Preliminary low-resolution data, not shown here, reveal that fluorescence extends for more than 3–4 mm, far from the beam axis. On the other hand, the fluorescence signal has a peak of about 25-nsec FWHM followed by a much weaker and longer (150-nsec) decay. This indicates that fluorescence is produced by particles moving with velocities of 10^4–10^5 m/s which cannot be attributed to ions escaping from the interaction region, but rather to the electrons that gained a kinetic energy equal to the ponderomotive energy in the laser electric field. While expanding, these electrons ionize Xe atoms and induce a contribution to the total fluorescence, mainly outside the interaction region. For an intensity $I=10^{14}$ W/cm^2, the electron velocity is around 1.5×10^6 m/s. At this energy the momentum transfer cross section between electrons and Xe atoms [28] is 3×10^{-15} cm^2, which, under our experimental conditions, yield an average time between collisions of 6 nsec and a diffusion coefficient of 5×10^7 cm^2/s. These are only rough estimations, but they assist us in building up the model. We must mention that in solving the equation for the plasma evolution, the inclusion of the diffusion term in Eq. (5) was necessary. We could not obtain a reasonable fit with measurements by considering only the advection term in Eq. (5) to describe the electron expansion. A recent study [29] of the propagation of laser generated plasma into low-pressure gases advanced a similar conclusion: computation that does not include diffusion effects can adequately describe only the earliest stage of plasma expansion into background gas.

We present in Fig. 8 the experimental and calculated transverse profiles of the fluorescence produced by 0.6 Torr of Xe, irradiated with 10-mJ, 35-fs laser pulses, for different positions of the input pinhole with respect to the focus. The observation point was at $z=5$ mm from the input pinhole. The equivalent data for an observation point at $z=50$ mm from the input pinhole are presented in Fig. 9.

As mentioned before, the parameters of the model are the diffusion constant D, the velocity v, and the initial electron distribution in the interaction region. To simulate the initial electron distribution we refer again to Fig. 13. In the fit we assumed a constant density n_0 for $r\leqslant r_0$, continued with a Gaussian distribution with a $1/e$ width equal to w_0, for $r>r_0$. In this way, the $z=5$ mm case and the $z=50$ mm case in Fig. 13 could be treated by setting $r_0\neq0$ and $r_0=0$, respectively. The values obtained for a best fit are presented in Table II for both $z=5$ mm and $z=50$ mm. They should be regarded as indicative parameters from which one can derive qualitative information about the kinetics of the plasma and the channel formation.

TABLE II. Values of the parameters obtained from fitting the transverse profile data. Both $z=5$ mm and $z=50$ mm data are given, in the form $(z=5)/(z=55)$.

z_L (cm)	r_0 (μm)	w_0 (μm)	$D\times10^6$ (cm^2/s)	$v\times10^8$ (cm/s)	n_0^{fit}	n_0^{theor}
0	0/40	150/130	52/35	5.0/2.0	92/38	92/38
15	0/40	150/130	43/30	4.2/1.9	58/25	78/28
25	0/0	150/180	25/26	3.0/1.9	37/15	48/18
35	0/0	150/180	20/22	2.0/1.9	12/5	22/10

For $z=5$ mm, the distribution of the electrons could be well fitted with a Gaussian of 150 μm $1/e$ width. The obtained width is in very good agreement with the calculated data in Fig. 13. Also, here $r_0=0$ because, as seen from Fig. 13, at $z=5$ mm we do not have a flat central distribution, and the channel formation occurs only after 4–5 cm of pulse propagation.

For $z=50$ mm, the top-hat distribution is clearly seen in the experimental data in Fig. 9 for $z_L=0$ and $z_L=15$ cm, and is reflected in the $r_0=40$-μm values obtained for these z_L values. The total width of the distribution $r_0+w_0=170$ μm is somewhat lower than the theoretical value (~250 μm) shown in Fig. 13. A first reason could be the overestimation of the ionization rates used for simulation. The higher the rates used, the larger the resulting channel diameter. However, the ionization rates yielded a good agreement in the calculation of the axial profiles of the fluorescence, so this does not seem to be the reason. We believe that the reason originates in the differences between the real laser beam (which is a truncated and focussed Gaussian) and the ideal Gaussian distribution which we used in the calculation. The particular mechanism of channel formation, as described above, is sensitive to the initial radial distribution of the laser intensity. Indeed, as mentioned earlier, the measured beam waist is around 210 μm, while we started the calculation with a theoretical value of 230 μm as estimated [30] from the iris diameter.

The values obtained for the diffusion coefficient and electron velocity provide additional information about the field configuration in the channel. For $z=5$ mm the calculated intensity on z axis decreases from 2×10^{14} W/cm^2 for $z_L=0$ to about half that for $z_L=35$. Correspondingly, the velocity parameter in the fit decreases from 5×10^8 cm/s to 2×10^8 cm/s. The diffusion coefficient also decreases in about the same proportion. For $z=50$, however, the field varies much more slowly with z_L, being around 10^{14} W/cm^2 for all cases. Accordingly, the v parameter is maintained practically constant at around 2×10^8 cm/s.

The diffusion coefficient is, in general, inversely propor-

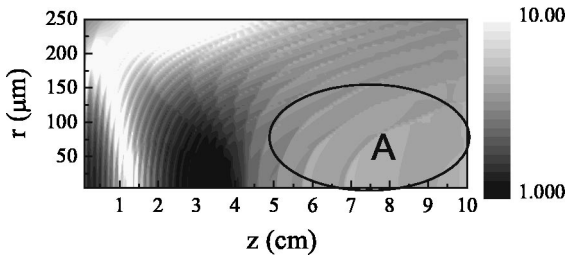

FIG. 14. Calculated 2D maps of the coherence lengths for the 13th harmonic in Xe. Intensity and phase of the fundamental field are taken from configuration (a) in Fig. 10.

tional to the pressure and directly proportional to (temperature)$^{3/2}$. This means it would decrease linearly with increasing electron concentration, and increase higher than linearly with increasing laser intensity. The overall trend is a decrease of D with increasing z_L, which is more pronounced for $z=5$ mm, where the variation of the laser intensity is stronger.

To clarify the relationship between channel formation and harmonic generation, we performed a phase-matching analysis using the graphical method of Balcou *et al.* [31]. For H13 in the case of Xe, we calculated the polarization wave vector as $\boldsymbol{k}_{pol}=13\boldsymbol{\nabla}[\phi_1(r,z)]+\boldsymbol{\nabla}[\alpha I(r,z)]$, where ϕ_1 is the fundamental field phase and α is the phase coefficient [32] for harmonics generated in the plateau. Following Ref. [31] we define a coherence length $L_{coh}=\pi/\delta k$ where $\delta k=2\pi q/\lambda-|\boldsymbol{k}_{pol}|$. We want to point out that $I(r,z)$ and $\phi_1(r,z)$ are here obtained from the calculated solution of the propagation equation, and *not* from the unperturbed fundamental field. The advantage of this procedure is that all the nongeometrical effects (dispersion, absorption, and ionization) are already included in L_{coh}, thus, one need not consider them separately as is usually done (see, for example, Ref. [33]). Once the propagated field is known, the above described calculation of the coherence length is a computationally inexpensive but useful approach to studying the harmonics generation. It avoids the lengthly calculation of the atomic polarization and harmonic field, while still giving valuable information about harmonic phase matching.

We calculated the coherence lengths for case (a) in Fig. 10. The 2D map in an (r,z) coordinate system is shown in Fig. 14. Only the central part is of interest for us, since for $r>250$ μm the field intensity vanishes. Also, the region of highest coherence length, observed around $z=1$ cm, is not interesting for us because the ionization level in this region, as seen from Fig. 10, is close to unity, and thus gas polarization will vanish. Our interest is in the region with $z>5$ cm and $r<200$ μm, where ionization is around 15% and the coherence lengths are high, being in general greater than 4 cm. We conclude that in this region (labeled A in Fig. 14), which corresponds to the channeled region in Fig. 10, harmonics generate and propagate under phase-matching conditions. This example clearly demonstrates the intrinsic link between the channel formation and the efficient generation of harmonics. The basic reason is that, in this region, both the intensity and the phase of the fundamental field exhibit almost no variation, either axially or radially. Region A has a large volume which means a high efficiency and a high harmonic energy. Also, it is topologically compact and situated close to the propagation axis, which means that the generated harmonics will generate and propagate close to the axis with low divergence.

Based on the mechanism of channeling formation, we can give a qualitative explanation for the data in Fig. 3. The decrease of the harmonic field with increasing the distance z_L between the input pinhole and the focusing lens can be explained as follows: the lower the intensity at the input pinhole, the smaller the radius for which Eq. (11) is satisfied. This can be clearly seen in the inset of Fig. 13. A slight decrease of the field intensity inside the channeled region, as z_L increases, can also contribute to the decrease in the harmonic field produced, however, we believe that the main effect is a volume effect. A complete calculation of the harmonic field could better estimate the relative importance of the two effects. However, we should mention here that $z_L=0$ might not be the optimum lens position in terms of conversion efficiency. We did not scan the lens positions for negative values of z_L, i.e., cell in the converging beam. The purpose of the present study was not to search for the optimum lens position but to reveal the relationship between channel formation and HH generation in the channel.

The dependence of the harmonic field intensity on the incident intensity for a constant z_L can also be explained in similar terms: the higher the incident intensity, the higher the radius of the formed channel. For example at $z=50$ mm, for Xe at 0.6 Torr, and $z_L=0$ (corresponding to the conditions in Fig. 12) the radii for which the intensity decreases by $1/e$ from its maximum are 255, 290, and 310 μm for incident energies of 7, 10, and 12 mJ, respectively. From 7 mJ to 12 mJ this represents an increase of almost 50% in the cross section. The average values of the intensity in the channel for these three pulse energies are 0.93, 1.04, and 1.08 $\times 10^{14}$ W/cm^2, respectively, thus, there is a much smaller variation.

The pulse propagated in Ar does not generate a self-guiding structure and for this case an even simpler and more practical 1D approach for the phase-matching calculation can be applied. As the ionization is sufficiently low to be negligible, balancing the Gouy phase of the unperturbed beam with the phase due to dispersion by neutrals proved to be sufficient to predict the optimum working pressure. Of course, as the ionization level increases, the phase-matching calculation should include its influence, as illustrated above.

V. CONCLUSION AND SUMMARY

In this experiment, we performed simultaneous measurements of plasma fluorescence and harmonic yield in Ar and Xe, in a long static cell at high pumping energies and loose focusing geometry, using 35-fs pulses from a Ti:sapphire laser. Axial and transverse profiles of the plasma column were measured under several experimental conditions with the aim of characterizing the pulse propagation. From the plasma fluorescence profiles we demonstrate that, under the given experimental conditions, pulse propagation in Xe is channeled. A 3D nonadiabatic propagation model was used to

calculate the field configuration in the interaction region and to explain the channel formation. A model developed to calculate the transverse plasma profiles can adequately reproduce the experimental data and confirm the channel formation. On the basis of the experimental results and simulation, we showed that channel formation greatly enhances the harmonic yield because in the channel propagate under phase-matched conditions.

On the other hand, the channeled plasma structure was not observed in the Ar case up to 20-mJ input energy. Since the input laser energy was limited by pump pulse SPM at the entrance window and focusing lens, the maximal input pump energy was set at 20 mJ. By using an input laser energy of higher than 20 mJ without the SPM effect, we may expect to generate higher energy HH and channeling structures under the phase-matched condition.

ACKNOWLEDGMENTS

This research was supported by Grant-in-Aid for Scientific Research on Priority Areas No. 14077222, by a grant from The Kurata Memorial Hitachi Science and Technology Foundation, and by The Special Postdoctoral Researchers' Program of RIKEN.

[1] K. Ishikawa and K. Midorikawa, Phys. Rev. A **65**, 043405 (2002).
[2] K. Nakajima and L.A.A. Nikolopoulos, Phys. Rev. A **66**, 041402(R) (2002).
[3] A.D. Bandrauk and S. Chelkowski, Phys. Rev. Lett. **87**, 273004 (2001).
[4] U. Saalmann and J.-M. Rost, Phys. Rev. Lett. **89**, 143401 (2002).
[5] V. Ayvazyan *et al.*, Phys. Rev. Lett. **88**, 104802 (2002).
[6] A. McPherson, G. Gibson, H. Jara, U. Johann, T.S. Luk, I.A. McInstyre, K. Boyer, and C.K. Rhodes, J. Opt. Soc. Am. B **4**, 595 (1987).
[7] M. Ferray, A. L'Huillier, X.F. Li, L.A. Lompre, G. Mainfray, and C. Manus, J. Phys. B **21**, L31 (1988).
[8] M. Hentschel, R. Kienberger, C. Spielmann, G.A. Reider, N. Milosevic, T. Brabec, P. Corkum, U. Heinzmanns, M. Dreschers, and F. Krausz, Nature (London) **414**, 509 (2001).
[9] E. Takahashi, Y. Nabekawa, T. Otsuka, M. Obara, and K. Midorikawa, Phys. Rev. A **66**, 021802(R) (2002).
[10] E. Takahashi, Y. Nabekawa, M. Nurhuda, and K. Midorikawa, J. Opt. Soc. Am. B **20**, 158 (2003).
[11] E. Takahashi, Y. Nabekawa, and K. Midorikawa, Opt. Lett. **27**, 1920 (2002).
[12] J.-F. Hergott, M. Kovacev, H. Merdji, C. Hubert, Y. Mairesse, E. Jean, P. Breger, P. Agostini, B. Carre, and P. Salières, Phys. Rev. A **66**, 021801(R) (2002).
[13] C. Dolle, C. Reinhardt, P. Simon, and B. Wellegehausen, Appl. Phys. B: Lasers Opt. **B75**, 629 (2002).
[14] D. Yoshitomi, T. Shimizu, T. Sekikawa, and S. Watanabe, Opt. Lett. **27**, 2170 (2002).
[15] E. Constant, D. Garzella, P. Berger, E. Mevel, C. Dorrer, C.L. Blanc, F. Salin, and P. Agostini, Phys. Rev. Lett. **82**, 1668 (1999).
[16] D.G. Lee, H.T. Kim, K.H. Hong, C.H. Nam, I.W. Choi, A. Bartnik, and H. Fiedorowicz, Appl. Phys. Lett. **81**, 3726 (2002).
[17] E. Priori, G. Cerullo, M. Nisoli, S.D. Silvestri, P. Villoresi, L. Poletto, P. Ceccherini, C. Altucci, R. Bruzzese, and C. de Lisio, Phys. Rev. A **61**, 063801 (2000).
[18] M. Amosov, N. Delone, and V. Krainov, Zh. Eksp. Teor. Fiz. **91**, 2008 (1986).
[19] E. Esarey, P. Sprangle, J. Krall, and A. Ting, IEEE J. Quantum Electron. **33**, 1879 (1997).
[20] B. LaFontaine, F. Vidal, Z. Jiang, C. Chien, D. Comtois, A. Desparois, T. Johnston, J. Kiefer, H. Péepin, and H. Mercure, Phys. Plasmas **6**, 1615 (1999).
[21] K.C. Kulander, Phys. Rev. A **38**, 778 (1988).
[22] C. Siders, G. Rodriguez, J. Siders, F. Omenetto, and A. Taylor, Phys. Rev. Lett. **87**, 263002 (2001).
[23] S. Augst, D. Meyerhofer, D. Strickland, and S. Chin, J. Opt. Soc. Am. B **8**, 858 (1991).
[24] R. Rankin, C.E. Capjack, N. Burnett, and P.B. Corkum, Opt. Lett. **16**, 835 (1991).
[25] A. Sergeev, M. Lontano, M. Chernobrovtseva, and A. Kim, in *Applications of High Field and Short Wavelength Sources*, edited by L. DiMauro, M. Murnane, and A. L'Huillier (Plenum, New York, 1998), p. 207.
[26] A. Sergeev, M. Lontano, A. Kim, V. Gildenburg, M. Chernobrovtseva, V. Pozdnyakova, and I. Shereshevskii, Laser Part. Beams **17**, 129 (1999).
[27] V. Gildenburg, N. Zharova, and M. Bakunov, Phys. Rev. E **63**, 066402 (2001).
[28] S. Hunter, J. Carter, and L. Christophorou, Phys. Rev. A **38**, 5539 (1988).
[29] H. Le, D. Zeitoun, J. Parisse, M. Sentis, and W. Marine, Phys. Rev. E **62**, 4152 (2000).
[30] E. Siegman, *Lasers* (University Science, Mill Valley, CA, 1986).
[31] P. Balcou, P. Salières, A. L'Huillier, and M. Lewenstein, Phys. Rev. A **55**, 3204 (1997).
[32] M. Lewenstein, P. Salières, and A. L'Huillier, Phys. Rev. A **52**, 4747 (1995).
[33] L. Roos, E. Constant, E. Mevel, D. Deschamps, M. Gaarde, A. Valette, R. Haroutunian, and A. L'Huillier, Phys. Rev. A **60**, 5010 (1999).